Numerical simulations of fluid flows and heat transfer in melt pools of Directed Energy Deposition of SS316L

Zaki Saldi[1,2,*], *Tim* Pasang[3], *Winston* Khogres[4], *Arief* Budiman[5,6,7], *Fergyanto* Gunawan[5]

[1]Department of Product Design, Universitas Pembangunan Jaya, Tangerang Selatan, 15413, Indonesia
[2]Center for Urban Studies, Universitas Pembangunan Jaya, Tangerang Selatan, 15413, Indonesia
[3]Department of Engineering Design, Manufacturing and Management Systems, Western Michigan University, Kalamazoo, 4900-5200, MI, USA
[4]Business Engineering Program, Industrial Engineering Department, BINUS ASO School of Engineering, Bina Nusantara University, Jakarta, 11480, Indonesia
[5]Industrial Engineering Department, BINUS Graduate Program - Master of Industrial Engineering, Bina Nusantara University, Jakarta, 11480, Indonesia
[6]Department of Manufacturing and Mechanical Engineering and Technology, Oregon Institute of Technology, Klamath Falls, 97601, OR, USA
[7]Oregon Renewable Energy Center (OREC), Klamath Falls, 97601, OR, USA

Abstract. This paper presents the numerical model developed to simulate fluid flow and heat transfer in melt pools formed in Directed Energy Deposition of stainless steel SS316L. The model incorporated important heat and momentum source terms. The energy source terms included laser energy, latent heat of phase change, convective heat loss, radiative heat loss, evaporative heat loss, and energy addition due to molten particle deposition into the melt pool. The momentum source terms were due to surface tension effect, thermocapillary (Marangoni) effect, thermal buoyancy, momentum damping due to phase change, molten particle momentum, and recoil effect due to evaporation. The simulations suggested that the predicted flow and heat transfer in the melt pool affected the resulting shape and size. With the process parameters currently employed, the melt pool was elongated, wide and shallow, with depressed free surface and outward convective flow. The outward flow was caused by the dominant region of high temperature in the centre of the melt pool, such that the temperature gradient of surface tension is negative.

1 Introduction

Directed Energy Deposition (DED) is an emerging manufacturing process of metallic components that has been applied in many different fields, e.g. aerospace [1-4], automotive [5-8], and biomedical engineering [9-12]. The capability of DED includes the creation of complex geometries and structures with high precision [13]. Moreover, its potential

* Corresponding author: zssaldi@gmail.com

application in sustainable remanufacturing of metallic components is also highlighted by successful repair of defective voids in turbine blades with 45% carbon footprint improvement as compared with total part replacement [14].

Despite its big potential and added values to design, manufacturing, and remanufacturing, DED still suffers from challenges that may hinder its practical application and reliability. First, the high energy input required can lead to thermal distortions and residual stresses in the final product [15]. Second, the limited material compatibility restricts the range of applications for DED processes [16]. Other factors that demand careful consideration include the precision and quality control of the deposited layers, which can affect the mechanical properties and dimensional accuracy of the finished product [17].

To tackle these challenges, parameters that control the DED process need to be optimized. The parameters include, among others, laser power, laser speed, and powder feed rate, the selection of which also needs to be based on the chosen print material. DED relies on an external heat source that continuously melts a stream of metallic powder or wire deposited into the molten part of the sample, referred to as melt pool. The deposition through the formation of melt pool proceeds on a layer-by-layer basis until the final shape is obtained. In pursuit of optimizing the process parameters, numerical simulations using Computational Fluid Dynamics (CFD) are essential to gain an understanding of various physics involved in DED. At the mesoscale, CFD is particularly useful to study the formation and evolution of the melt pool, which is subjected to a complex dynamics of fluid flow and heat transfer that involve various driving forces. Such dynamics influence the overall temperature gradient and cooling rates in the printed sample as well as many other variables, which are prohibitively expensive or even not possible to be measured experimentally. These variables have an important consequence on the microstructure evolution of the printed component, which will eventually determine its mechanical properties. Therefore, CFD can be employed as numerical experiments to test a range of process parameters applied to gain an understanding of the underlying mechanisms of the resulting microstructure and properties of the DED-printed component. Based on this workflow, an optimum range of parameters can be selected with more confidence.

Based on the above motivation, the objectives of this paper are: (i) To perform CFD simulations to predict fluid flows and heat transfer in the melt pools formed in a single-layer DED process; and (ii) To study the effect of heat and fluid flow on the melt pool shape and size. As a case study, stainless steel SS316L was used to demonstrate the model applicability.

2 Numerical model and setup

The typical DED process is illustrated in Fig.1, in which the metallic powder flowing from a feeder is deposited on the base substrate through heating and melting. The energy required to heat and melt the powder is provided by laser beam / electron beam / electric arc. As the molten metal is deposited, melt pool is also formed, which is illustrated in Fig. 2, where laser beam is used as the energy source. The laser moves in the scanning direction, where it continuously supplies energy to the melt pool. Various phenomena occurring in the melt pool include heat transfer in the modes of conduction, convection, and radiation; phase changes (melting, solidification, and evaporation); as well as fluid flows induced by surface tension gradients (Marangoni effect), thermal buoyancy, and free surface oscillations. Altogether, the driving forces drive the fluid flows and transfer energy from the melt pool to the surrounding substrate area. The heat transfer affects the microstructure in the heat-affected zone. Behind the melt pool, cooling takes place and results in the solidified bead. As the process repeats at the next layer, remelting happens and the subsequent layer is fused with the layer below it as they solidify, and thermal cycles develop during the whole DED build.

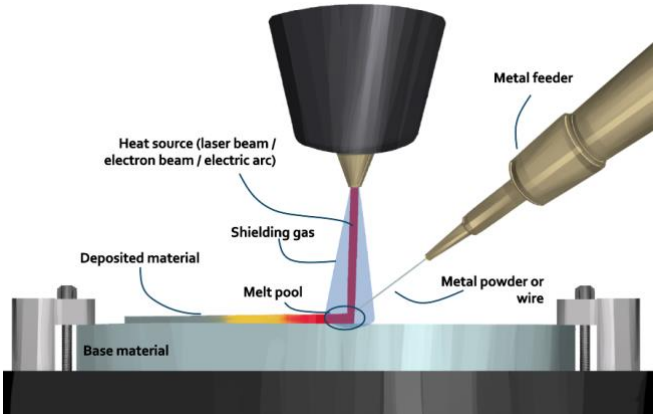

Fig. 1. Illustration of a typical Directed Energy Deposition (DED) process.

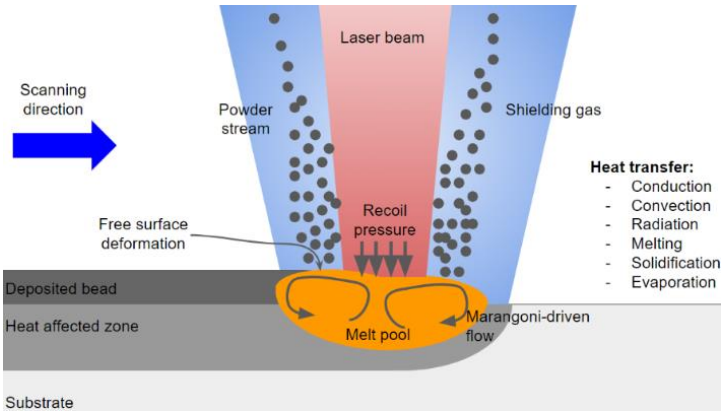

Fig. 2. Various phenomena occurring in the melt pool.

This section outlines the numerical model that was developed to simulate heat transfer and fluid flows in the melt pool. The governing equations are explained, and the source terms are highlighted. Next, the properties and process parameters used in the simulation are described. The settings in the simulation are also summarized.

2.1 Numerical model

The numerical model is based on the conservation laws of mass (continuity), momentum of viscous fluid (Navier-Stokes), and energy, expressed as follows, respectively.

$$\frac{\partial \rho}{\partial t} + \nabla \cdot (\rho \boldsymbol{U}) = \dot{M} \tag{1}$$

$$\frac{\partial}{\partial t}(\rho \boldsymbol{U}) + \nabla \cdot (\rho \boldsymbol{U}\boldsymbol{U}) = -\nabla p + \nabla \cdot (\mu \nabla \boldsymbol{U}) + \boldsymbol{S}_U \tag{2}$$

$$\frac{\partial}{\partial t}(\rho H) + \nabla \cdot (\rho \boldsymbol{U} H) = \nabla \cdot (k \nabla T) + q_H \tag{3}$$

In the above conservation equations, ρ is the density, t time, $\boldsymbol{U}$ velocity vector, $\dot{M}$ rate of metallic particle mass addition per unit volume, p pressure, μ dynamic viscosity, $\boldsymbol{S}_U$ momentum source term, H total enthalpy, k thermal conductivity, T temperature, and q_H energy (heat) source term.

The free surface of melt pool, i.e. interface between the melt pool and the gas phase above it, was captured using the Volume of Fluid (VoF) method, in which the transport equation of volume fraction F was solved. The volume fraction of 1 corresponds with the main phase (solid and liquid metal), whereas 0 denotes the secondary phase (gas). The free surface of the metal is represented by volume fraction range bounded by 0 and 1. The VoF transport equation is expressed as

$$\frac{\partial F}{\partial t} + \nabla \cdot (\boldsymbol{U}F) = \dot{F} \quad (4)$$

The term $\boldsymbol{S}_U$ in Eq. (2) is the sum of 6 momentum source terms, i.e. damping momentum corresponding to phase change $\boldsymbol{S}_{PC}$, momentum due to thermal buoyancy $\boldsymbol{S}_{TB}$, momentum due to surface tension effect $\boldsymbol{S}_{ST}$, momentum due to surface tension gradient (Marangoni) effect $\boldsymbol{S}_{MF}$, momentum due to molten particle deposition $\boldsymbol{S}_P$, and momentum due to recoil force $\boldsymbol{S}_{RF}$:

$$\boldsymbol{S}_U = \boldsymbol{S}_{PC} + \boldsymbol{S}_{TB} + \boldsymbol{S}_{ST} + \boldsymbol{S}_{MF} + \boldsymbol{S}_P + \boldsymbol{S}_{RF} \quad (5)$$

The energy source term q_H appearing in the energy conservation equation (Eq. (3)) is due to the external heat source (laser) q_L, latent heat in phase change q_{PC}, convective heat loss q_{conv}, radiative heat loss q_{rad}, evaporative heat loss q_{evap}, and particle heat q_P:

$$q_H = q_L + q_{PC} + q_{conv} + q_{rad} + q_{evap} + q_P \quad (6)$$

The momentum and heat source terms above will not be explained in details here, and can be found from literature [18]. The fluid flow and heat transfer in the melt pool formed during DED based on the numerical model outlined above was simulated using CFD software ANSYS Fluent 2020R2. As some of the terms and parameters were not available in the released version of the software, they were implemented into the software by programming the corresponding formula through User-defined Function (UDF).

2.2 Material properties and process parameters

The above model was employed to simulate metal deposition over a line track in a single layer DED of SS316L with helium as the shielding gas, as shown in Fig. 3. The track length was 3 mm, with the laser initially positioned at x = 3.5 mm from the edge of the base material.

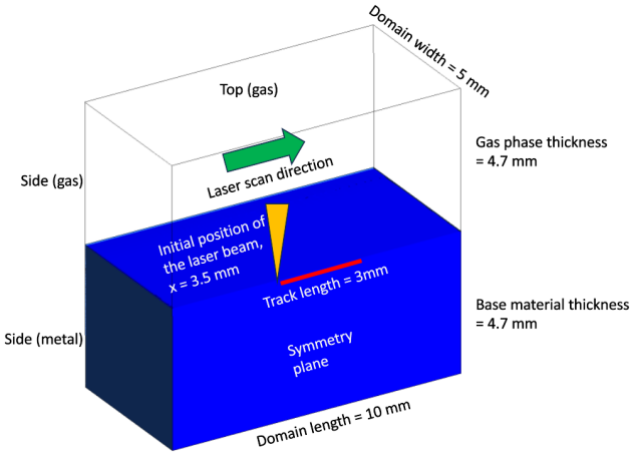

Fig. 3. Schematic of DED process studied.

The material properties are based on the values taken from literature [19] and the main DED process parameters are summarized in Table 1. UDF was also programmed to model temperature-dependent material properties, i.e. thermal conductivity, specific heat, surface tension, and dynamic viscosity.

Table 1. The process parameters used in the simulations.

Process parameters	Value	Unit
Laser power	500	W
Laser spot diameter	1.2	mm
Laser scanning speed	10	mm/s
Metal powder feeding rate	10	gr/min
Powder absorption efficiency into the melt pool	0.95	-

2.3 Simulation settings

Fig. 3 also shows the computational domain used in the simulation, with the length of 10 mm, width 5 mm, and thickness of each phase 4.7 mm. At t = 0 s, volume fraction of 0 and 1 was set in the gas phase and base material, respectively. A symmetry boundary condition was imposed at the central plane parallel to the path of the laser beam translation. Adiabatic boundaries were applied at the side and bottom surfaces of the base material, whereas pressure outlet conditions were set at the top and side boundaries of the gas phase. The laser beam and metal feeder were positioned coaxially, such that they move at the same scanning speed as listed in Table 1. The beam and feeder movement were implemented in UDF.

The conservation equations were discretised using the Finite Volume Method (FVM). The 1st-order implicit Euler scheme was applied to the time-derivative terms, while 2nd-order upwind was applied to the convective fluxes. Adaptive time stepping method tailored for multiphase simulation was used with a time step of 10^{-6} s applied for the first 10 time-marching iterations. The under-relaxation factor of 0.3 was used for pressure and 0.7 for momentum vectors. Convergence criterion for the residual of linear equation matrix iteration was set at 10^{-4}, 10^{-5}, and 10^{-6} for continuity, momentum, and energy, respectively. PISO algorithm was used for the treatment of the pressure-velocity coupling. Using sensitivity analysis, a structured hexahedral mesh with 448,800 elements was selected as it offered a good compromise between simulation time and mesh-independence of the numerical solutions.

3 Results and discussion

Based on the CFD simulation, the predicted melt pools represented by their temperature and velocity fields can be plotted. Fig 4 shows the melt pools time evolution when viewed from the symmetry plane, whereas Fig 5 shows the melt pools at the axial y-z plane. The planes shown at each time instance in Fig 5 are the corresponding planes of the position of the laser beam centre point.

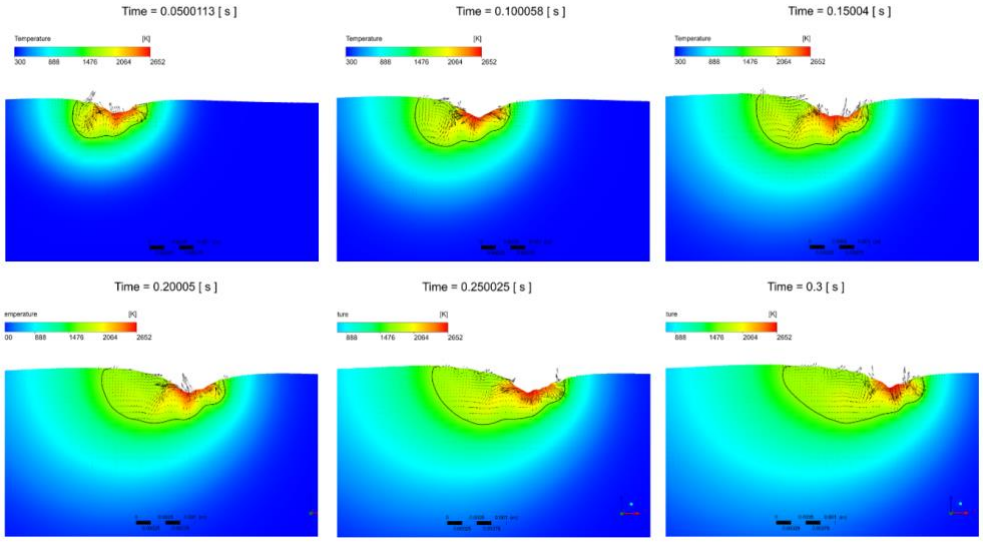

Fig. 4. The melt pools represented by temperature and velocity fields at the symmetry plane, from t = 0.05 to 0.3 s, with time increment of 0.05 s.

The results in Fig. 4 and 5 show that free surface was deformed, which was caused by the combination of surface tension, thermocapillary (Marangoni) effects, and mass addition due to molten metallic particles. Furthermore, there are several characteristics that can be observed from the melt pool free surface, to be explained as follows.

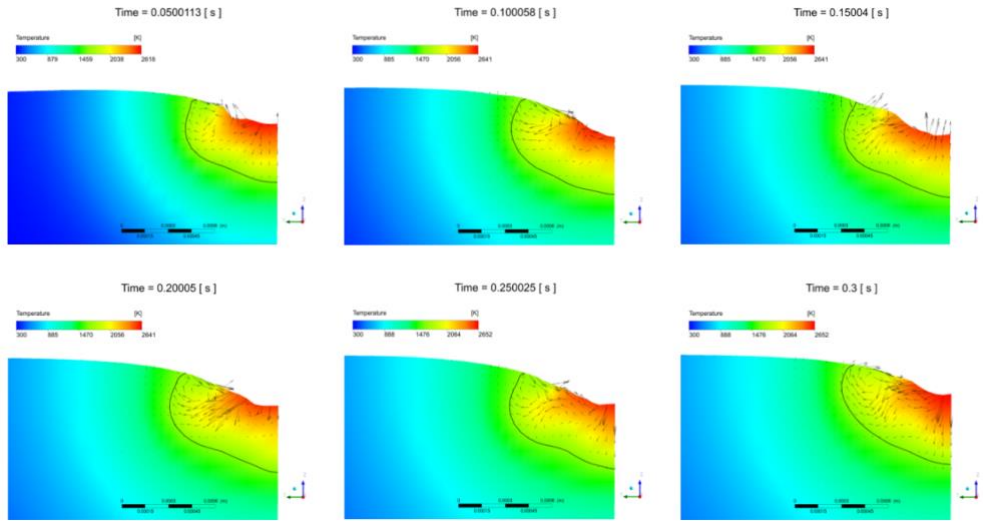

Fig. 5. The melt pools represented by temperature and velocity fields at y-z plane, from t = 0.05 to 0.3 s, with time increment of 0.05 s.

First, the maximum temperature was around 2500-2600 K, which is higher than the evaporation temperature of SS316L. This is likely due to the active heat and momentum sources corresponding to the metallic particle deposition in the melt pool. At the same time, due to evaporation, recoil pressure occurred, pushing the free surface downward.

Second, the region of high temperature at the free surface is quite significant. This could result from the interplay between all heat and momentum sources due to molten particle deposition. Moreover, there was a tendency of the melt to flow outward in the centre region of the free surface. The outward flow also helped spread out the thermal energy at the free surface. The outward flow itself was attributed to the thermocapillary (Marangoni) effect driven by the profile of temperature gradient of surface tension. With the addition of molten metallic particle energy, the surface temperature increased such that it exceeded the critical temperature where the sign of temperature gradient of surface tension changes from positive to negative. For SS316L, this transition temperature is around 2200 K. The temperature in the periphery of the melt pool lies below this temperature, which means that the temperature gradient of surface tension is positive. This resulted in the flow in the direction of increasing temperature (inward). On the contrary, the temperature in the centre of the melt pool is higher than the critical temperature and the temperature gradient of surface tension is negative. Therefore, the flow is in the direction of decreasing temperature (outward).

The Marangoni phenomena can also explain the effects of flow direction on the melt pool shape. As the surface region with temperature higher than the critical temperature is significant, the outward flow from the centre prevails over the inward flow from the edge. This outward flow carried more thermal energy to melt the pool edge, such that it pushed the melting/solidification boundary further downstream and sideways, effectively causing elongated, wide, and shallow melt pool.

Table 2 outlines the dimension of the melt pools as they were evolving in the simulations. The dimension was characterized by melt pool length, depth, and width, extracted from t = 0.05 s to 0.3 s, with time increment of 0.05 s.

Table 2. Dimensions of the melt pools from t = 0.05 s to 0.3 s, with time increment of 0.05 s.

Time (s)	Length (mm)	Depth (mm)	Width (mm)
0.05	1.137	0.576	1.104
0.1	1.546	0.704	1.249
0.15	1.816	0.76	1.376
0.2	1.918	0.728	1.402
0.25	2.111	0.766	1.389
0.3	2.244	0.744	1.459

Table 2 also shows quantitatively that although the melt pool tends to expand due to the incoming laser energy, the size also fluctuates sometimes. The fluctuation in melt pool shape and size can also be seen in Fig. 4 and 5. This indicates that the fluid flow and heat transfer in the melt pool is highly unsteady, which can be attributed to the complex interplay between various source terms, in combination with the non-linear material properties and process parameters. Therefore, the numerical model and simulations illustrated in this paper play an important role in gaining insight into the complexity of the melt pool, which would guide process parameter optimization in the long term.

4 Summary

This paper addresses numerical modelling and simulation of melt pools in Directed Energy Deposition (DED) for 3D-printed metallic parts, specifically focusing on stainless steel SS316L. The study employs Computational Fluid Dynamics (CFD) to develop a numerical model, incorporating various source terms. The energy source terms included laser energy, latent heat of phase change, convective heat loss, radiative heat loss, evaporative heat loss, and energy addition due to molten particle deposition into the melt pool. The momentum source terms were due to surface tension effect, thermocapillary (Marangoni) effect, thermal buoyancy, momentum damping due to phase change, molten particle momentum, and recoil effect due to evaporation. The simulations reveal important insights into the flow, heat transfer, and resulting shape and size of the melt pools.

The examination of temperature and velocity fields in the melt pools elucidates the influence of evaporation, thermocapillary effects, and energy addition from molten metallic particles. Due to energy addition from molten metallic particles, the maximum temperature at the free surface is higher than the evaporation temperature, contributing to surface depression due to recoil pressure. The energy addition also increased the temperature such that it exceeded the critical temperature where the sign of temperature gradient of surface tension changed from positive to negative. This Marangoni effect explains the dominating outward flow in the centre of the melt pool and its impact on pool shape. Quantitative analysis of the melt pool shape and size showed that the outward flow resulted in elongated and wide, but shallow, melt pools.

While the numerical simulations provide valuable insights, it must be noted that the current study still needs to be further complemented by experimental measurements, which can also validate the findings and analysis in this paper. The next stage in the research will include post-solidification measurement of the melt pool shapes formed in DED of SS316L, along with process parameter variation. CFD simulations of melt pools formed in DED thus can provide valuable baseline for achieving desired melt pool characteristics, microstructure, and mechanical properties in 3D-printed metallic parts.

The authors would like to thank DRTPM (Directorate of Research, Technology and Community Service), The Ministry of Education, Culture, Research and Technology (Kemendikbudristek) for the research grant support (contract number 410/LL3/AK.04/2022, 17 June 2022).

References

1. A. Suárez, F. Veiga, T. Bhujangrao, E. Aldalur, J. Mater. Eng. Perform. **31**, 6270-6282 (2022)
2. J.C. Najmon, S. Raeisi, A. Tovar, Addit. Manuf. Aerospace Ind. , 7-31 (2019)
3. A. Pathania, S.A. Kumar, Mater. Today: Proc. **45**, 4886-4892 (2021)
4. S. P. Kumar, Mater. Today: Proc. **46**, 7892-7906 (2021)
5. R. Sampson, R. Lancaster, M. Sutcliffe, D. Carswell, C. Hauser, J. Barras, Opt. Laser Technol. **134**, 106609 (2021)
6. J.C. Vasco, Addit. Manuf. Handb. Adv. Manuf., 505-530 (2021)
7. N. Zhao, M. Parthasarathy, S. Patil, D. Coates, K. Myers, H. Zhu, W. Li, J. Manuf. Syst. **68**, 368-375 (2023)
8. J. Bennett, D. Garcia, M. Kendrick, T. Hartman, G. Hyatt, K. Ehmann, F. You, J. Cao, J. Manuf. Sci. Eng. **141**, Issue 2 (2019)

9. T. Bhardwaj, M. Shukla, Lasers Manuf. Mater. Process. **7**, 245 - 258 (2020)
10. T. Bhardwaj, M. Shukla, C.P. Paul, K.S. Bindra, J. Alloys Compd. **787**, 1238-1248 (2019)
11. J. Shinjo, C. Panwisawas, Addit. Manuf. **51**, 102654 (2022)
12. D.J. Ryu, H.Y. Ban, E.Y. Jung, C.H. Sonn, D.H. Hong, S. Ahmad, B. Gweon, D. Lim, J.H. Wang, J. Clin. Med. **9**, 478 (2020)
13. K.S.B. Ribeiro, F.E. Mariani, R.T. Coelho, Procedia Manuf. **48**, 663-670 (2020)
14. J.M. Wilson, C. Piya, Y.C. Shin, F. Zhao, K. Ramani, J. Clean. Prod. **80**, 170-178 (2014)
15. M. Liu, A. Kumar, S. Bukkapatnam, M. Kuttolamadom, Procedia Manuf. **53**, 507-518 (2021)
16. T. Lehmann, D. Rose, E. Ranjbar, M. Ghasri-Khouzani, M. Tavakoli, H. Henein, T. Wolfe, A.J. Qureshi, Int. Mater. Rev. **67**, Issue 4 (2022)
17. D.S. Shim, G.-Y. Baek, J.-S. Seo, G.-Y. Shin, K.-P. Kim, K.-Y. Lee, Opt. Laser Technol. **86**, 69-78 (2016)
18. Z. Sun, W. Guo, L. Li, Addit. Manuf. 33, 101175 (2020)
19. R.H. Bogaard, P.D. Desai, H.H. Li, H.H, C.Y. Ho, Thermochim. Acta, **218**, 373-393 (1993)